

Computational Verification and Experimental Validation of the Vibration-Attenuation Properties of a Geometrically Nonlinear Metamaterial Design

Journal Article

Author(s):

Chondrogiannis, Kyriakos Alexandros ; Colombi, Andrea ; Dertimanis, Vasilis; Chatzi, Eleni 

Publication date:

2022-05

Permanent link:

<https://doi.org/10.3929/ethz-b-000549998>

Rights / license:

[In Copyright - Non-Commercial Use Permitted](#)

Originally published in:

Physical Review Applied 17(5), <https://doi.org/10.1103/PhysRevApplied.17.054023>

Funding acknowledgement:


813424 - INNOVATIVE GROUND INTERFACE CONCEPTS FOR STRUCTURE PROTECTION (EC)

863179 - Bio-Inspired Hierarchical MetaMaterials (EC)

174009 - Structured materials for multiscale wave control (SNF)

Computational Verification and Experimental Validation of the Vibration-Attenuation Properties of a Geometrically Nonlinear Metamaterial Design

Kyriakos Alexandros Chondrogiannis^{✉,*}, Andrea Colombi[✉], Vasilis Dertimanis[✉], and Eleni Chatzi[✉]
Department of Civil, Environmental and Geomatic Engineering, ETH Zurich, Stefano-Franscini-Platz 5, Zurich 8093, Switzerland

 (Received 16 January 2022; revised 2 April 2022; accepted 5 April 2022; published 13 May 2022)

To prevent the severe effects of earthquake on built systems, structural engineering pursues attenuation of vibrations on structures. A recently surfaced means to structural vibration mitigation exploits the concept of metamaterials, i.e., of configurations able to control wave propagation in specific frequency ranges, termed band gaps. The current study harnesses the potency of a geometrically nonlinear unit-cell design, which can develop negative stiffness, and explores the vibration-attenuation capabilities of the resulting metamaterial device. An analytical approach is followed to calculate the expected attenuation zone, as well as for calculating the dependence on the amplitude of the input, a hallmark of the nonlinear behavior. For the purpose of validation of a proof-of-concept system, dynamic tests are performed on a scaled model assembled using LEGO[®] components. Besides showing that such a nonlinear system can be easily constructed, these tests illustrate the potential of this nonlinear design for vibration reduction within the targeted band-gap frequency zones and the protection that it can offer to a primary system. Finally, numerical analyses are used to verify the analytical calculations of the dispersion relation and are additionally compared to the experimental results, evaluating the incorporated modeling assumptions. The possibility to lower the band gap in the typical seismic engineering frequency range and to maintain a broadband attenuation at low frequency show that negative stiffness may enhance the performance of metamaterials for seismic protection.

DOI: [10.1103/PhysRevApplied.17.054023](https://doi.org/10.1103/PhysRevApplied.17.054023)

I. INTRODUCTION

Control and attenuation of mechanical vibrations has formed a major challenge in the domain of structural engineering. Dynamic loads, such as earthquakes and explosions, influence and compromise the capacity and safety of engineering structures [1]. This subject becomes, particularly challenging for civil-engineering applications, where the primary source of undesired vibration stems from seismic excitation [2], or is tied to resonance effects that comprise a spectral content that lies in the lower-frequency range (1–20 Hz).

Structural vibration attenuation is extensively treated via base-isolation techniques [1,3] or with the attachment of passive, active, and semiactive devices [4,5]. Perhaps the most exploited form of a passive vibration-attenuation device, in the structural engineering context, are the tuned mass and tuned liquid dampers [6–9], which comprise additional, linear attachments to the primary system. While this application is particularly effective, when tuned to

the—typically first—natural frequency of the protected structure, it affects only a narrow frequency band. On the other hand, active and semiactive devices come with the significant drawback, when compared against passive solutions, of requiring power supply, incurring higher costs, and frequent maintenance, while exhibiting vulnerability to sensor and actuator failures [10].

A vibration-mitigation concept that is proposed, yet rapidly evolving, for engineering applications is that of metamaterials [11–13]. These are structures that are arranged in a repeating pattern of a fundamental design, called the unit cell. They exhibit remarkable filtering properties when placed in the direction of propagation of waves, within specific frequency regions that are called band gaps. Two types of mechanisms are identified, underpinning the dynamic behavior of metamaterials, namely Bragg scattering and local resonance [14,15]. Resonant metamaterials exploit a principle that is similar to the tuned mass damper concept; the tuning of the natural frequency of each cell to a specified value around which a band gap is formed. On the other hand, the Bragg-scattering mechanism exploits destructive interference between periodic unit cells for preventing the propagation of waves at

*Chondrogiannis@ibk.baug.ethz.ch

wavelengths approximately equal to the spacing between adjacent cells [16–18].

One of the most investigated linear designs for structural protection are mass-in-mass resonant metamaterials [19,20]. Common applications of such designs include so-called metafoundation and metabarrier concepts [21–25]. Barriers are placed in the surrounding medium of the superstructure, without the requirement to thus bear its weight. To this end, Miniaci *et al.* [26] show the potential of a metabarrier against seismic surface waves in reducing ground motion. Metafoundations, on the other hand, are placed beneath the structure as a support system, thus bearing its weight. In a structural-focused direction, Wenzel *et al.* [27] study the protection of storage tanks with the use of resonant metafoundations clearly revealing the attenuation capabilities in the resulting stresses.

Here we claim that major limitations of linear metamaterials such as the high mass necessary to reach low frequencies and the limited frequency band of the attenuation zone can be overcome adopting a nonlinear unit-cell design. Furthermore, the inherent amplitude-dependent behavior may result in adaptation of the band-gap range, depending on the magnitude of the oscillation [28]. Several studies in the recent literature integrate metamaterial concepts to mild nonlinear configurations [29–36] studying their tunability properties, while others investigate the effect of nonsmooth phenomena [37–39], revealing the benefits in terms of larger attenuation bandwidths that can be obtained by exploiting nonlinearities.

To this end, negative stiffness phenomena are very promising for vibration isolation and can be generated by harnessing geometric nonlinearities. In this direction, Hwang *et al.* [40] study the dynamic behavior of a metabeam design with bistable asymmetric elements. Al-Shudeifat and Chen *et al.* [41,42] investigate the effects of nonlinear energy sinks with a negative stiffness element, showing promising results. This latter concept helps towards focusing the attention on the potential advantages of negative stiffness for elastic metamaterials. Wenzel *et al.* [28], Chen *et al.* [43], and Salari-Sharif *et al.* [44] propose unique metamaterial designs incorporating negative stiffness unit cells, revealing the potential of such systems towards structural protection. In a similar spirit, the K-Damper concept [45–47] aims at vibration isolation, utilizing negative stiffness elements, taking into consideration the bearing capacity in the vertical direction, therefore maintaining a positive overall stiffness.

Building on existing knowledge, this study proposes a geometrically nonlinear metamaterial pursuing response reduction at low frequency. Contrary, for instance, to the K-Damper concept, this system allows the overall stiffness of the unit cells to become negative by targeting lateral (and not vertical) support. The band gap and its dependence on the nonlinear mechanism is explained by means of analytical and numerical techniques. To further

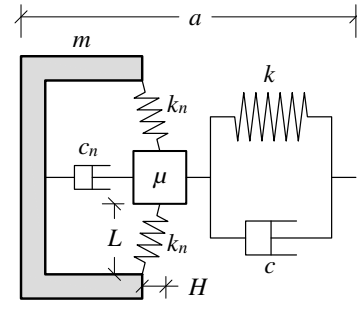


FIG. 1. Schematic representation of the geometrically nonlinear unit cell.

validate the proposed design in a scaled proof of concept, experimental tests are performed under dynamic loading.

II. GEOMETRICALLY NONLINEAR UNIT CELL

The metamaterial design investigated in the current work enforces geometrically nonlinear behavior at the unit-cell level. Its design is similar to the works of Al-Shudeifat [41] and Chen *et al.* [42], depicted in Fig. 1. It consists of a rigid support of mass m , connected to a mass μ via a nonlinear element. The nonlinear kinematics is induced by a triangular arch configuration, that consists of two linear springs of stiffness k_n arranged in an isosceles triangle geometry of height H and base of length $2L$, as shown in Fig. 2. Each unit cell of lattice constant a ; in other words, the length of each cell, is elastically connected to the adjacent cells via a linear spring of stiffness k . Damping is considered both in the nonlinear element and in the link between cells via linear dashpot elements of coefficients c_n and c , respectively.

A triangular arch that undergoes large displacements is known to yield a geometrically nonlinear behavior with a bistable configuration, as discussed in the work of Chen *et al.* [42]. Figure 2 displays the resting position of the arch and the corresponding equilibrium path of this setup. The two linear springs of stiffness k_n have a natural length L' and are assembled in a triangular geometry of height H .

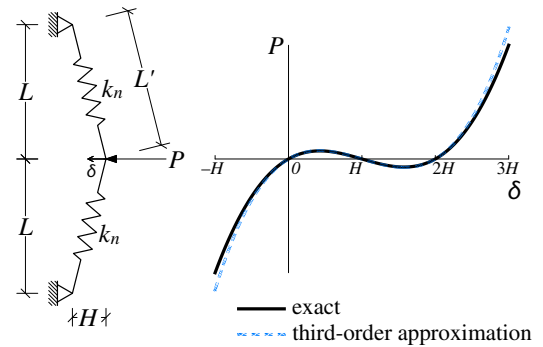


FIG. 2. Nonlinear equilibrium path of the triangular arch.

While the presence of nonlinearity is apparent, the behavior that is produced is elastic as the loading and unloading paths are identical. Two stable equilibrium points can be identified for $\delta = 0$ and $\delta = 2H$, that correspond to the two symmetrical positions at which the springs are at their natural length. A third unstable equilibrium point occurs at $\delta = H$, where the two springs are aligned, while being compressed. Equation (1) states the exact equilibrium path of the setup as a function of geometric and stiffness properties of the individual components. This relation is approximated with a third-order polynomial function, in order to simplify the analytical derivation, after performing a Taylor series expansion around $\delta = H$ [41], as formulated in Eq. (2). The deviation of the approximated relation from the exact path is shown in Fig. 2, where sufficient agreement is observed. This deviation is $\leq 10\%$ for the displacement range $(-H, 3H)$, while it is increased for outer values. The oscillation amplitudes in the following sections are expected to fall within this displacement range and therefore this approximation can offer useful indications about the dynamic behavior of the system.

$$P = 2k_n L' \left(1 - \sqrt{\frac{(L/H)^2 + [1 - (\delta/H)]^2}{(L/H)^2 + 1}} \right) \times \frac{1 - (\delta/H)}{\sqrt{(L/H)^2 + [1 - (\delta/H)]^2}}, \quad (1)$$

where $L' = \sqrt{L^2 + H^2}$.

$$\begin{aligned} P &\approx k_1 (\delta - H) + k_2 (\delta - H)^3, \\ k_1 &= -2k_n \left(\frac{L'}{L} - 1 \right), \\ k_2 &= \frac{k_n L'}{L^3}. \end{aligned} \quad (2)$$

III. ANALYTICAL DERIVATION OF THE DISPERSION RELATION

A first indication on the filtering properties of a metamaterial design is obtained via the study of the dispersion curves. In analytical terms, this aims at determining the real solutions to the dispersion relation obtained for an infinite chain [48,49]. Imaginary solutions represent evanescent waves that do not propagate through the lattice. These may be used to distinguish between Bragg and local resonance band gaps. The infinite lattice involves a periodic arrangement that consists of an infinite number of unit cells. This consideration eliminates the uniqueness of each cell and therefore enables the study of an arbitrary set of $j, j-1, j+1$ cells [50–52], exploiting periodicity and allowing the assumption of periodic boundary conditions.

The dispersion relation is typically computed by applying periodic boundary conditions [53–55] on the cell edges

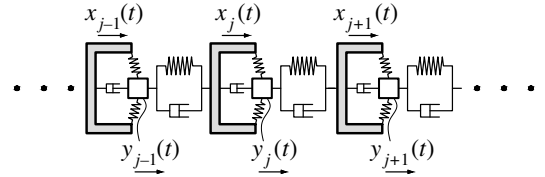


FIG. 3. Schematic representation of the theoretical infinite lattice.

[28,56–60] to mimic an infinite, perfectly periodic chain as depicted in Fig. 3.

The relative displacement of the two masses of the j th unit cell, is defined as v_j , which reads

$$v_j(t) = x_j(t) - y_j(t), \quad (3)$$

where $x_j(t)$ and $y_j(t)$ are the displacements of mass m and μ of the j th cell, respectively.

The equations of motion for the j th unit cell, in absence of damping, read

$$\begin{aligned} m\ddot{x}_j + k(x_j - x_{j-1} + v_{j-1}) + F_j^{\text{nl}} &= 0, \\ \mu(\ddot{x}_j - \ddot{y}_j) + k(x_j - v_j - x_{j+1}) - F_j^{\text{nl}} &= 0, \end{aligned} \quad (4)$$

where F_j^{nl} denotes the interaction between the nonlinearly connected masses of the j th cell. This force-displacement relation of the nonlinear element in Eq. (5) is assumed to follow the simplified relation of Eq. (2), centered around $\delta = H$.

$$F_j^{\text{nl}} = k_1 v_j + k_2 v_j^3. \quad (5)$$

The solutions to the equations of motion then assume the following form [28]:

$$\begin{aligned} x_{j\pm 1}(t) &= (U_1 e^{i\omega t} + \bar{U}_1 e^{-i\omega t}) e^{\pm iq}, \\ v_{j\pm 1}(t) &= (V_1 e^{i\omega t} + \bar{V}_1 e^{-i\omega t}) e^{\pm iq}, \end{aligned} \quad (6)$$

where ω is the angular frequency, q is the reduced wave number ($q = \kappa a$, κ is the wave number), $i = \sqrt{-1}$ is the imaginary unit, and \bar{V}, \bar{U} denote complex conjugates.

Substitution of Eq. (6) into Eq. (4), and application of the harmonic balance method [61], by balancing the terms of $e^{i\omega t}$, result into the dispersion relation of the system in Eq. (7).

$$\begin{aligned} \cos(q) &= [2k(k_1 + 3k_2 V_1 \bar{V}_1) \\ &\quad - (m + \mu)(k + k_1 + 3k_2 V_1 \bar{V}_1)\omega^2 + m\mu\omega^4] \\ &\quad / [2k(k_1 + 3k_2 V_1 \bar{V}_1)]. \end{aligned} \quad (7)$$

In contrast to linear metamaterial solutions, the behavior of this nonlinear system depends on the oscillation amplitude

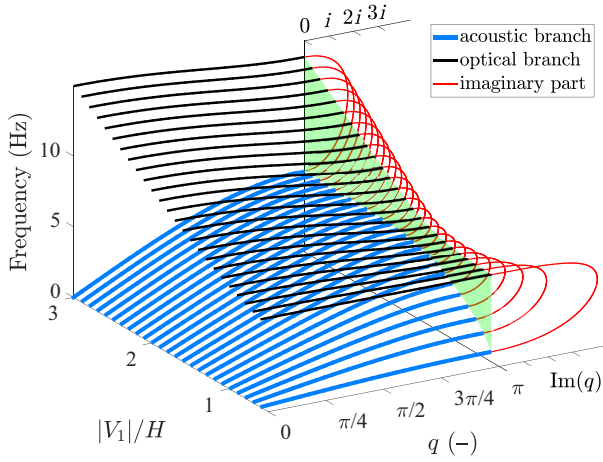


FIG. 4. Graphical representation of the dispersion curves, obtained via analytical calculations. Green color indicates the evolution of the band gap in the amplitude-frequency space. ($m = 2$, $\mu = 1$, $k_n = 2 \times 10^3$, $k = 10^3$, $H = 0.15$, $L = 0.5$.)

through the term $V_1 \bar{V}_1$ in Eq. (7). V_1 is defined in Eq. (6) as the amplitude of the relative displacement of the nonlinearly connected masses of the cell and $V_1 \bar{V}_1 = |V_1|^2$. In order to calculate the dispersion relation, $|V_1|$ should be defined, leading to the relation between frequency and wave number. Thus, for each predefined value of $|V_1|$, Eq. (7) is solved analytically for discrete wave-number values, yielding the respective solutions for the frequency. This is performed with symbolic operations in the MATLAB[®] symbolic environment, where for a given wave number and amplitude value the frequency satisfying the relation in the real domain is part of the dispersion curves. A similar procedure for given frequency and amplitude values determines the imaginary part of the solution.

Figure 4 illustrates this dispersion relation. It is a three-dimensional representation that includes the additional dependence on the relative oscillation amplitude between

the nonlinearly connected masses of each unit cell. The acoustic and the optical branches [62] are formed, which define the boundaries of the band gap for the infinite chain. Since both branches are affected by the dependence on amplitude, the band gap not only shifts to different frequency but also changes its width. For lower amplitudes, it tends towards lower frequencies, while for higher ones it shifts toward higher-frequency ranges. Limited amplitudes allow the triangular arch to oscillate at reduced angles, thus creating a flexible element, while higher amplitudes force the arch to form sharper angles, resulting into a subsequent stiffening of the setup. Additionally, it is observed that for lower amplitudes, the acoustic branch is significantly altered compared to the optical one that experiences minor alterations, while for higher amplitudes the opposite behavior is observed. The study of the imaginary part of the solution reveals additional information on the amount of attenuation inside the band gap and further confirm the Bragg origin of the band gap (smooth and rounded curve shape). It is observed that for low and high oscillation amplitudes this attenuation is significantly increased compared to intermediate amplitudes (around $|V_1| = H$).

IV. EXPERIMENTAL TESTS

A. DESCRIPTION OF THE SETUP

The dynamic behavior of the investigated metamaterial configuration is studied experimentally. For this purpose, a scaled physical model is created and tested under dynamic loading. Figure 5 depicts the developed experimental setup. Previous studies on various linear and nonlinear metamaterial designs [21,35] suggest that even for a reduced number of unit cells (two–three) a substantial band gap can be generated, leading to noticeable motion reduction. Significant vibration mitigation is evident even for a single layer of the nonlinear metafoundation design with negative stiffness in the work of Wenzel *et al.* [28]. This

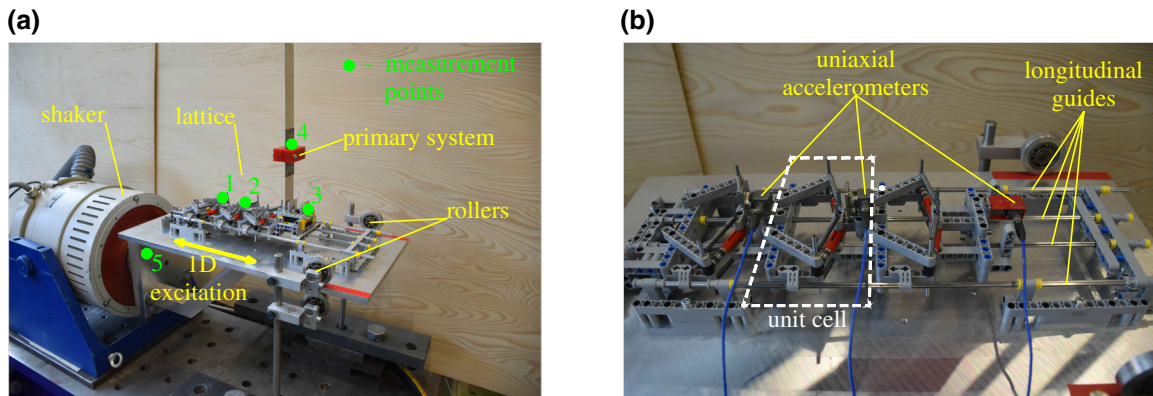


FIG. 5. Experimental setup. (a) Overview of the configuration testing the device mounted at a primary system. (b) Closer depiction of the setup without a protected structure.

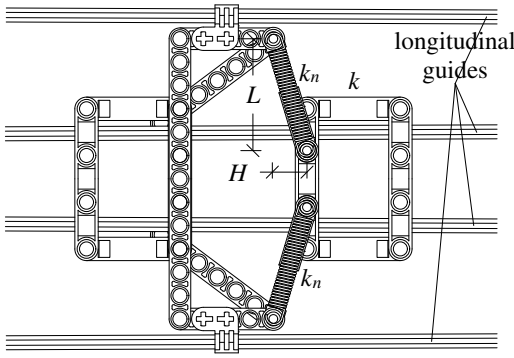


FIG. 6. Bottom view of the physical unit-cell design, used in the experimental configuration.

is essential for a realistic experimental implementation, where dimensions are limited.

An electrodynamic shaker applies a one-dimensional (1D) input excitation in a horizontal direction, as depicted in Fig. 5(a). An aluminum table is mounted to the shaker's shaft on one side, while on the other it is supported by rollers. This is to maintain the table in a leveled position as well as to limit parasitic vertical oscillations.

The metamaterial model is mounted on the shaking table and consists of three repeated nonlinear unit cells, whose kinematics is analogous to the design described in Sec. II. Each cell is formed by a stiff support to which the nonlinear element is connected, as shown in Fig. 6. The geometrically nonlinear element is formed by a triangular arch that consists of linear springs. Longitudinal guides ensure that displacements develop primarily in the desired direction, while lubricant liquid minimizes the effect of friction between the guides and the support. Apart from this minimal inevitable friction, the cells are completely detached from the shaking table. The input is applied to the left end of the chain, where the support of the first cell is mounted to the shaking table, creating longitudinal waves that propagate within the lattice. The proposed metamaterial design is tested using two different configurations; a first one featuring a primary system that should be isolated, at the end of the lattice while in a second case, the lattice is free at the right end, as shown in Fig. 5. Apart from the longitudinal guides that are made of aluminum to increase vertical and lateral rigidity, most of the metamaterial components are assembled using LEGO® parts.

The dynamic response of the system is measured using 1D accelerometers with a sampling frequency of 2 kHz. Uniaxial accelerometers are preferred over triaxial ones because of their reduced dimensions and weight. The measuring locations include each unit cell (measurements $\ddot{x}_{1,2,3}^{\text{ex}}$), the primary system (measurement \ddot{x}_4^{ex}), if present, as well as the shaker input signal (measurement \ddot{x}_5^{ex}), as seen in Fig. 5(a).

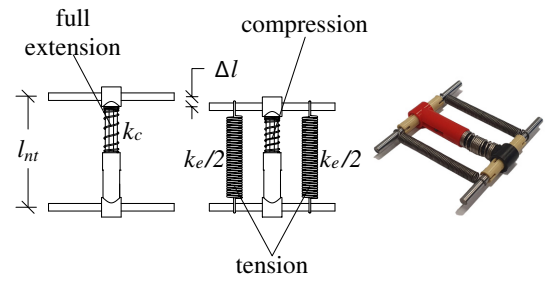


FIG. 7. Assembly of the linear stiffness elements at rest: (left) original, (center) modified configuration, (right) physical assembly.

To ensure that the nonlinear triangle works properly in both compression and extension, two additional coils of stiffness $k_e/2$ are installed to the LEGO® linear spring of stiffness k_c to keep the latter in a prestressed state, as shown in Fig. 7. The additional components shift the stable equilibrium position backwards by Δl . This allows the system to react equivalently in both the compression and extension states, in contrast to the original configuration, which is at full extension at its equilibrium position. The overall stiffness of the assembly k_n is therefore calculated as

$$k_n = k_e + k_c. \quad (8)$$

Table I summarizes the characteristics of the two types of unit cells that are used in the model. These are varying both in terms of the stiffness value k_n , as well as in terms of the geometry of the triangular arch, as a result of different natural lengths of the spring assemblies.

The shaker is controlled by a signal generator that can create different input signals. It can produce both sinusoidal inputs as well as sine sweeps, by controlling the voltage signal of the shaker. Figure 8 shows the frequency content of a measured sample sine-sweep signal that is applied. This signal, imposed by the shaker, results to a nearly flat spectrum for a given frequency range, thus exciting uniformly this specified range.

The efficiency of the metamaterial device is evaluated upon its attenuation capabilities on the primary system. The latter consists of a cantilever beam vertically oriented, attached to a base of mass M_{base} and a concentrated mass M_p , mounted to a specific height of the beam, as shown in Fig. 5(a) and schematically illustrated in Fig. 9. The dynamic characterization of the primary system is performed by studying its impulse response, as shown in

TABLE I. Geometric and stiffness characteristics of the different types of the experimentally tested unit cells.

Unit cell type	L (mm)	H (mm)	k_n (N/m)
A	40	11	1441
B	40	2	600

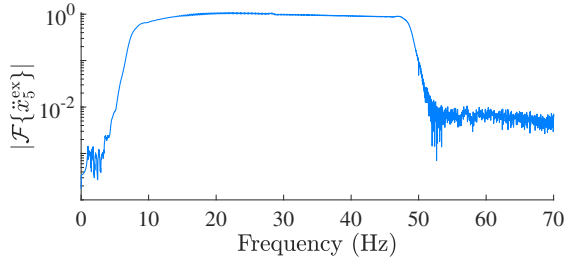


FIG. 8. Fourier spectrum of measured sine-sweep input (\ddot{x}_3^{ex}) sample in the range of 6–50 Hz.

Fig. 9. Two modes can be spotted with resonance frequencies $f_{n1} = 7.95$ Hz and $f_{n2} = 38.14$ Hz, respectively. For the tests with no protected structure, a mass M_s is attached to the last unit cell of the lattice, consisting of the accelerometer and its supporting structure shown in Fig. 5(b).

The mass properties of the individual elements of the metamaterial lattice and the primary system, including the mass of the corresponding sensors, are summarized in Table II. In the experimental setup $k \gg k_n$, therefore the connection between consecutive unit cells is practically rigid. This has the consequence of shifting the optical branch in Fig. 4 to higher frequencies, outside the range explored in this experiment. Therefore, the mass of each unit cell can be lumped as $m_{\text{cell}} = m + \mu$, as the distribution of m and μ within the cell has no effect on the observable dynamic response.

B. EXPERIMENTAL RESULTS

This section discusses the obtained experimental results. This series of tests includes inputs of sine-sweep excitation as well as single-harmonic inputs.

Figure 10 shows the frequency content of the response at the end of the lattice \ddot{x}_3^{ex} (mass M_s) for the free end

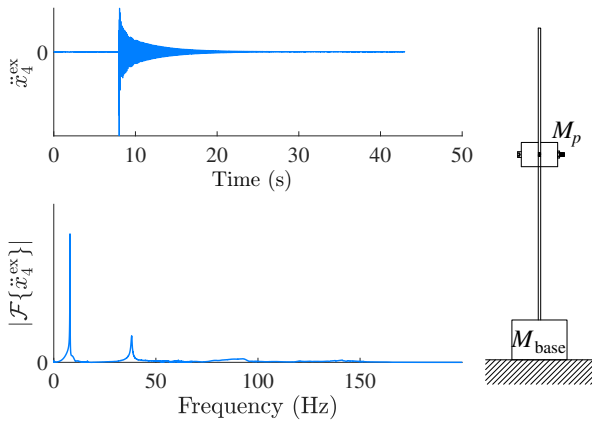


FIG. 9. Impulse response of primary system: (right) primary system, (top) acceleration time history, (bottom) fast Fourier transform.

TABLE II. Mass measurements for the individual parts of the experimental model.

Element	Mass (g)
M_p	111
M_{base}	143
M_s	89
m_{cell}	75

system in Fig. 5(b), with respect to the input \ddot{x}_5^{ex} . The system is excited with a sine-sweep input excitation, while the two types of unit cells are studied. The attenuation zone of the tested metamaterial device corresponds to the regions where the ratio of the frequency content between output and input falls below unity. This attenuation zone is observed for the various tests that are performed. As discussed, the acoustic part of the dispersion relation is explored, as the optical branch corresponds to much higher frequencies, which are not studied herein. Therefore, in this low-frequency regime, only the opening frequency of the band gap is spotted, where for lower values' wave propagation is not prohibited and for higher ones attenuation is present. Above a specific threshold, different in each tested configuration, the output is reduced with respect to the input, as indicated by the region of the figure where the ratio is lower than 1. As unit cell type *A* is stiffer than *B*, due to both the larger stiffness constant k_n as well as to the sharper angle of its triangular arch, the attenuation zone is driven to higher frequencies when compared against type *B*. This reduction zone additionally depends on the oscillation amplitude, as discussed in Sec. III. As expected, the higher the amplitude of the input acceleration the higher the opening frequency of the attenuation zone will be. Because of the equivalent stiffening of the triangular arch, experiencing sharper angles at higher oscillation amplitudes, this is apparent in both the softer and the stiffer unit-cell variations. Moreover, the reduction of the response varies depending on the oscillation amplitude. This is in line with the attenuation characteristics inside the band gap, as calculated in Sec. III.

It is further interesting to compare the attenuation zone formed with the two types of cells, focusing for example at high input acceleration (dashed lines). It is observed that this is additionally dependent on the amplitude of oscillations, as noted in Fig. 10. Although unit cell type *A* has a significantly higher initial stiffness than *B* the created band-gap opening frequency is not proportionally increased, because the cell oscillates at amplitudes smaller than H , as determined by the prediction of the analytical calculations of Sec. III. This results in a lower equivalent stiffness under dynamic conditions compared to the initial stiffness in the static state. This can be useful to

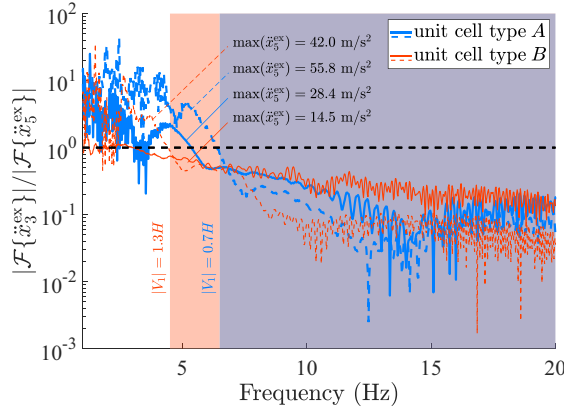


FIG. 10. Frequency content of the response at point 3 (mass M_s) for a lattice with a free end and sine-sweep excitation input. The maximum acceleration of the sine-sweep input for each test is denoted as $\max(\ddot{x}_5^{\text{ex}})$. The analytical band gap is depicted in solid color for each type of unit cell and corresponding oscillation amplitude.

vibration isolation applications where a certain static stiffness is required, while under dynamic loading this stiffness can be decreased and even become negative, thus preventing vibration from affecting a protected structure.

The response of the primary system both when attached to a fixed base and when isolated with the nonlinear metamaterial *A* and *B* is now investigated. A limitation arises due to the maximum displacement span that the shaker is able to apply. Therefore, the experimental range for the nonlinear system is bounded and depends on both the frequency (in the lower range) and the acceleration (for higher amplitude), which must result in displacements smaller than the capacity of the shaker.

Figure 11 depicts the acceleration response of the primary mass M_p for the setup of Fig. 5(a) and single-harmonic excitation. It is observed that all metamaterial configurations are able to offer reduction in the acceleration response of the primary mass compared to the fixed base case. This effect is not limited to the resonance frequency but it spreads on a wider range. Due to the aforementioned displacement limitations, the response in the lower-frequency range cannot be tested. In agreement with Sec. III, high excitation amplitudes result in stronger reduction, compared to intermediate input amplitudes, of the output to input ratio within the attenuation zone. It is further noted that the lattice with unit cell type *B* offers greater acceleration reduction around the resonance frequency of the protected structure, while for higher frequencies the effect of the two types appears to be similar, which is possibly relevant to the high mass of the primary system compared to the mass of the unit cells.

The peak visible in the acceleration response for the isolated cases at frequencies around 9 Hz has an interesting origin. At this frequency, there exists a resonance of the

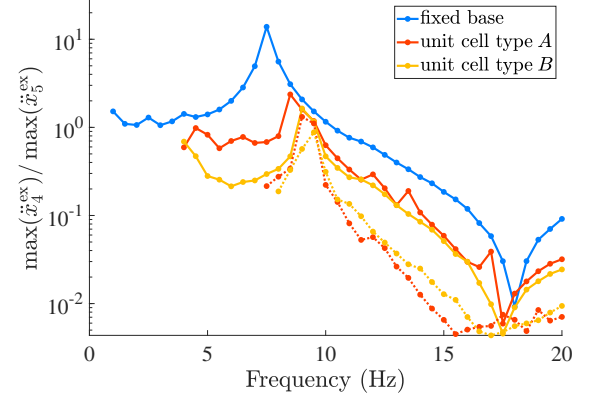


FIG. 11. Experimental results of the acceleration amplitude at the primary mass M_p for a sine excitation. For the models where the metamaterial lattice is present, solid lines correspond to input acceleration amplitude 10 m/s² and dashed lines to 30 m/s², respectively.

longitudinal guides and the primary system in the vertical direction. This phenomenon has two consequences. The first is the interaction between the flexural vibration of the primary mass and strong oscillations in the vertical direction. The second and most significant effect is the high friction that is produced between the sliding base of the primary system and the longitudinal guides. Vertical oscillations result to larger contact forces in this direction and therefore higher friction forces. The sliding base is not able to move independently of the guides and thus, the behavior of the primary system resembles the fixed-base case, as the displacements at the base of the protected structure approximate these of the input excitation. Indeed, from Fig. 11 it can be observed that when these peaks occur they closely follow the response of the fixed-base results.

The metamaterial device proves successful in limiting the response of the primary system in the tested frequency ranges. Crucially, accelerations around the resonant frequency of the primary system are substantially mitigated, as a result of the created band gap. Additionally, the amplitude dependence of the nonlinear behavior is evident. Higher input amplitudes lead to higher reduction of the response, in contrast to the primary, linear system. It is further observed that the device is able to mitigate vibrations across a broad frequency range, due to the location of the optical branch at high frequencies.

V. NUMERICAL SIMULATIONS

Following the analytical calculations of Sec. III and the experimental tests of Sec. IV, numerical simulations are now introduced. The finite lattice of identical unit cells in Fig. 12 is simulated numerically, while an external excitation is applied. Analytical solutions of the dispersion curves are first compared to the numerical simulations for a large chain, approximating the infinite lattice, while

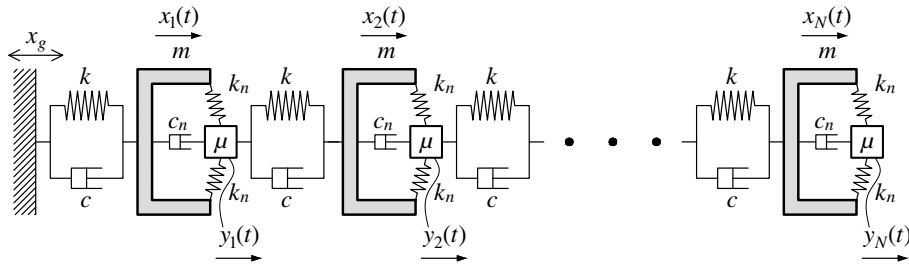


FIG. 12. Schematic representation of a finite lattice consisting of N unit cells, used for the numerical estimation of the dispersion relation.

experimental measurements of the three-cell setup are further compared to the numerical analyses in terms of time history response.

A considerable factor in the experimental tests is the friction that exists between the elements of each cell and the longitudinal guides of the setup. The latter, being fixed to the shaking table, follow the displacement of the input x_g in the longitudinal direction.

In the current study, friction is taken into consideration following a smooth Coulomb friction model [63], as shown in Fig. 13. The friction relationship is described by Eq. (9).

$$\text{Fr}(u) = c_g \tanh(c_v u), \quad (9)$$

where u denotes the relative velocity between two sliding bodies.

In the following sections, the dynamic motion of the lattice in Fig. 12 is simulated numerically in MATLAB® environment, by the solution of the equations of motion, with the use of *ode45* function (AbsTol = eps, RelTol = eps^(2/3), MaxStep = 10⁻², eps corresponding to the machine precision epsilon). To that end, the system is formulated in a nonlinear state-space representation:

$$\begin{aligned} \dot{z}(t) &= g(z(t), x_g(t)), \\ z &= [x_1, \dot{x}_1, y_1, \dot{y}_1, \dots, x_N, \dot{x}_N, y_N, \dot{y}_N]^T, \end{aligned} \quad (10)$$

where x_j and y_j are the displacements of masses m and μ of each cell j ($1 \leq j \leq N$), respectively.

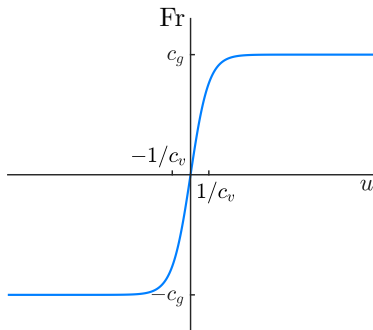


FIG. 13. Smooth Coulomb friction model.

The equations of motion of the first unit cell take the form:

$$\begin{aligned} m\ddot{x}_1 + c(\dot{x}_1 - \dot{x}_g) + c_n(\dot{x}_1 - \dot{y}_1) + k(x_1 - x_g) + \text{Fr}_x^1 \\ + F_{\text{nl}}^1 &= 0, \\ \mu\ddot{y}_1 + c(\dot{y}_1 - \dot{x}_2) + c_n(\dot{y}_1 - \dot{x}_1) + k(y_1 - x_2) \\ + \text{Fr}_y^1 - F_{\text{nl}}^1 &= 0. \end{aligned} \quad (11)$$

The equations of motion of the j th unit cell ($1 < j < N$) take the form:

$$\begin{aligned} m\ddot{x}_j + c(\dot{x}_j - \dot{y}_{j-1}) + c_n(\dot{x}_j - \dot{y}_j) \\ + k(x_j - y_{j-1}) + \text{Fr}_x^j + F_{\text{nl}}^j &= 0, \\ \mu\ddot{y}_j + c(\dot{y}_j - \dot{x}_{j+1}) + c_n(\dot{y}_j - \dot{x}_j) \\ + k(y_j - x_{j+1}) + \text{Fr}_y^j - F_{\text{nl}}^j &= 0. \end{aligned} \quad (12)$$

The equations of motion of the final (N th) unit cell are, respectively, formed:

$$\begin{aligned} m\ddot{x}_N + c(\dot{x}_N - \dot{y}_{N-1}) + c_n(\dot{x}_N - \dot{y}_N) \\ + k(x_N - y_{N-1}) + \text{Fr}_x^N + F_{\text{nl}}^N &= 0, \\ \mu\ddot{y}_N + c_n(\dot{y}_N - \dot{x}_N) + \text{Fr}_y^N - F_{\text{nl}}^N &= 0, \end{aligned} \quad (13)$$

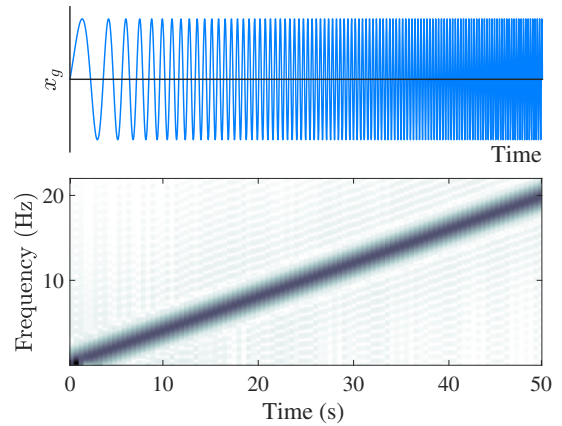


FIG. 14. Sine-sweep input excitation, used for the estimation of the dispersion curves, in the frequency range 0.1–20.0 Hz: (top) time history, (bottom) spectrogram, showing the output of the short-time Fourier transform.

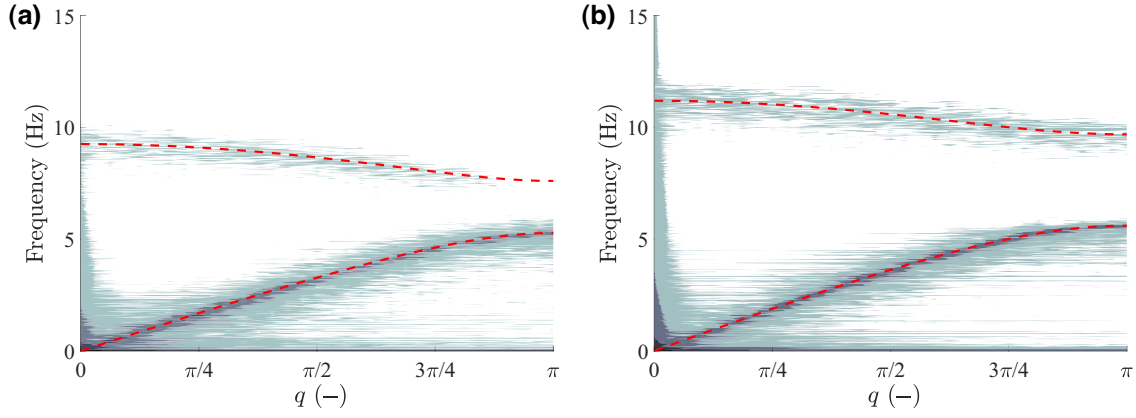


FIG. 15. Comparison of the numerical against the analytically computed dispersion curves for varying input amplitude. The contour plot corresponds to the numerical analyses and the dashed lines to the analytical solutions. (a) Intermediate input amplitude, $|V_1| = 1.6H$. (b) High input amplitude, $|V_1| = 2.1H$. ($m = 2$, $\mu = 1$, $c_n = 0$, $c = 0$, $c_g = 0$, $k_n = 2 \times 10^3$, $k = 10^3$, $H = 0.15$, $L = 0.5$, $N = 64$.)

where $F_{nl}^j = F_{nl}^j(v_j) = P(v_j)$, $v_j = x_j - y_j$. For these analyses, the exact formulation of the nonlinear equilibrium path of the triangular arch from Eq. (1) is used for the calculation of F_{nl}^j at each time step. Moreover, $Fr_n^j = Fr(u_j)$, $u_j = \dot{n}_j - \dot{x}_g$ and $n_j = x_j$ or y_j , respectively, denotes the friction between the elements of each cell and the longitudinal guides, according to Eq. (9).

A. NUMERICAL ESTIMATION OF THE DISPERSION CURVES

Additionally to the analytical derivations, numerical analyses are performed in order to approximate the dispersion relation of the system. For this purpose, a finite lattice, consisting of N identical cells is studied, as shown in Fig. 12. The system is excited by base excitation x_g , where evaluation on the respective wave-propagation behavior reveals useful dynamic properties.

Input is applied to the system in the form of base excitation x_g on one end of the lattice, as shown in Fig. 12. The input displacement is selected to follow a sine-sweep time history, plotted in Fig. 14, in the range of 0.1–20 Hz for a time period of 50 s. This wavelet has the property of uniformly exciting a specified frequency range by linearly varying its frequency content over time. This is depicted in the spectrogram of Fig. 14, where a short-time Fourier transform reveals the frequency content of the input with respect to time.

For the estimation of the dispersion curves via numerical analyses, the output signal should be studied. For the output states of the individual masses of each cell, a two-dimensional fast Fourier transform (FFT) in time and in space is applied [64]. In this section the displacement of mass m of each cell is used for the estimation of the curves. These outputs are plotted versus the corresponding reduced

wave number q and frequency in a contour plot, as shown in Fig. 15.

Figure 15 depicts the two-dimensional FFT of the output, which yields the numerical estimation of the dispersion curves for varying input excitation amplitude. Additionally, the corresponding analytical curves from Fig. 4, as calculated in Sec. III, are plotted. It is observed that the numerical results are in line with the analytical calculations. It is evident that the output in both approaches is dependent on the oscillation amplitude. The shifting of the dispersion curves and the corresponding band gap in the frequency domain appears in both analyses, enhancing their reliability. It is observed that high oscillation amplitudes result in a translation of the band gap to higher frequencies, while increasing its width.

B. NUMERICAL SIMULATION OF THE EXPERIMENTAL MODEL

In this section the response of the experimental model of Sec. IV is simulated numerically. It is helpful to compare the experimental results with numerical simulations. This can reveal the consistence in the assumptions of the numerical model that are in agreement with the analytical results, as discussed in Sec. V A.

In the physical model, it is not realistic to assume infinite rigidity in the supporting part (mass m) of the unit cell. In a more detailed analysis, the bending of the cantilever elements is incorporated, while the transverse element has much higher stiffness, taking into account the significantly larger cross section and thus assumed rigid, as shown in the left part of Fig. 16. As displacement δ evolves, it causes a corresponding shear load to the cantilever element at the joint, and therefore introduces a displacement r in the transverse direction. This process alters the force-displacement relation of this nonlinear configuration, thus

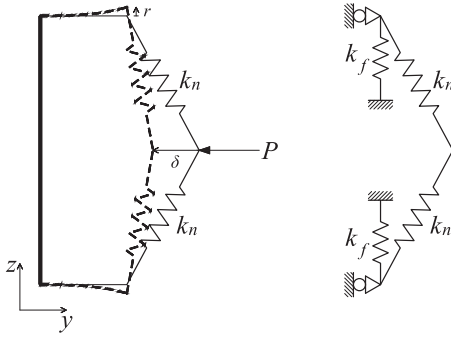


FIG. 16. (Left) Bending of the unit cell's supporting part. (Right) Equivalent stiffness representation.

shifting its properties. The stiffness of each cantilever element k_f can be converted to a linear spring, as sketched in Fig. 16.

In order to update the equilibrium path of Eq. (1) by incorporating the elasticity of the aforementioned elements, an incremental stepping algorithm is developed, as described in Appendix A.

Figure 17 shows the revised equilibrium path according to Eq. (A1), in comparison to the original solution of Eq. (1). It is observed that the updated force-displacement relation deviates from the original for an elastic support consideration, which can be a relevant factor of the dynamic behavior of the system.

To include the elasticity of the supporting members, their corresponding stiffness should be determined. For this purpose, the cantilever LEGO[®] element is simulated numerically with the use of linear finite-element analysis in ABAQUS[®] software. Figure 18 depicts the numerical model that is created, showing the boundary conditions, the applied load F , the resulting deformations, and the displacement measurement r .

Table III summarizes the material and calculated stiffness properties of the cantilever element.

The response of the physical model for the free end lattice, as described in Sec. IV, is here simulated numerically.

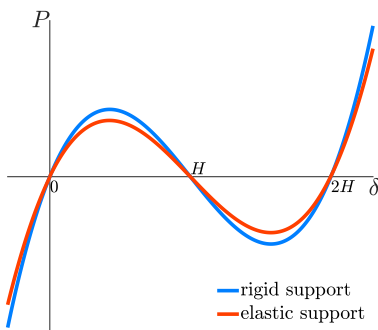


FIG. 17. Comparison of the nonlinear equilibrium path for a rigid and elastic support.

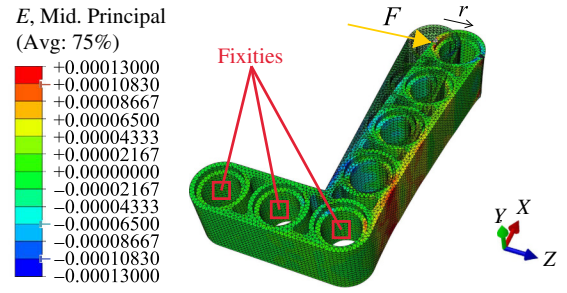


FIG. 18. FEA results of the deformed shape of the cantilever element under transverse load F triggering displacement r . This figure is produced with the ABAQUS[®] software.

This is performed for unit cell type A , for which the negative stiffness behavior is more pronounced. The parameters of the system are set following those of the actual model, as mentioned in Tables I–III. Additionally, as $k \gg k_n$ the constrain of $y_j = x_{j+1}$ for all unit cells is applied to the numerical model in Eq. (11)–(13), instead of selecting a high value for k , which would significantly increase the computational time. The friction model and damping parameters of the numerical simulations are calibrated, based on the experimental data, as $c_g = 0.35$, $c_v = 5$, and $c_n = 1.6$.

The dynamic response of the system is simulated numerically according to Eqs. (11)–(13). Figure 19 depicts the comparison of the numerical results to the experimental measurements of the acceleration at mass M_s (measurement point 3) for input excitation, the frequency content of which is shown in Fig. 8. Comparing the time history, considerable agreement is observed between the two types of output. Furthermore, the frequency content of the calculated response is compared to the one of the experimental measurements. The two outputs match closely for frequencies >6 Hz, as the ratio of their fast Fourier transform tends to 1. The sine-sweep input that is used does not include frequencies <6 Hz, therefore the discrepancy of the results in this region is not of concern. It is therefore concluded that the numerical model can offer a useful indication regarding the dynamic response of the nonlinear system.

The frequency response of the system is further studied. Single-harmonic input is applied to the system with constant acceleration amplitude of 30 m/s^2 . The response at the output is calculated numerically, and compared to the experimental measurements. The latter are limited to

TABLE III. Material (E , modulus of elasticity; ν , Poisson's ratio) [65] and calculated stiffness properties of the LEGO[®] cantilever element.

E	2.28 GPa
ν	0.41
k_f	$34.48 \times 10^3 \text{ N/m}$

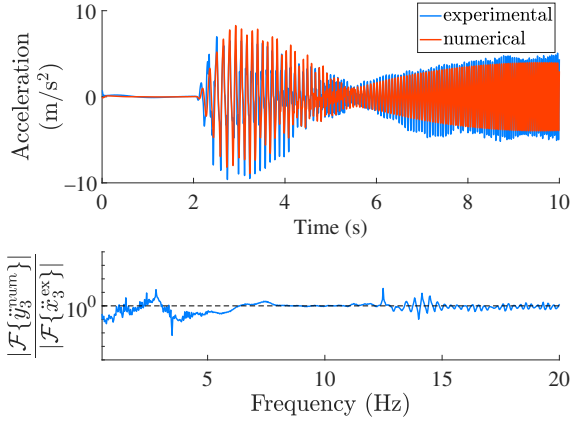


FIG. 19. Comparison of numerical to experimental results at mass M_s for sine-sweep excitation (unit cell type A). (Top) Acceleration time history, (bottom) ratio of frequency content.

a frequency threshold, due to the limitations discussed in Sec. IV B, while the numerical simulation further reveals the behavior of the response for lower frequencies, and in the propagative zone of the metamaterial. Figure 20 shows the comparison between the numerical analyses and experimental measurements of the output acceleration for discrete frequencies. The results are in agreement, for the frequencies where both analytical and experimental data are available. Discrepancies can be ascribed to the effect of friction, an admittedly nontrivial add on to a model that is already nonlinear in nature. To an extent, an improved approximation of the actual properties could be obtained by means of more sophisticated friction models. These could incorporate the discontinuity of the phenomenon, therefore increasing substantially the computational cost, in comparison to the smooth Coulomb friction model, used in this study, which is superior in numerical stability [63]. While these increase the computation time, the improvement in the approximation of friction would be limited and therefore the smooth Coulomb friction model is selected.

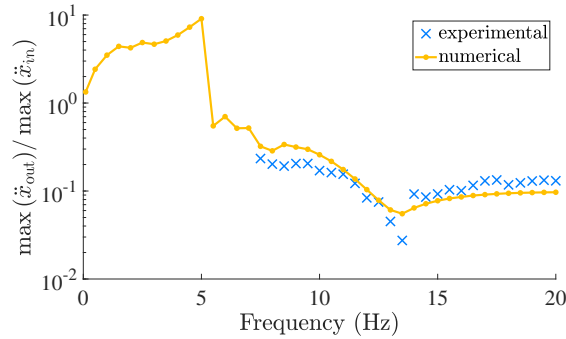


FIG. 20. Numerical and experimental results of the frequency response for single-harmonic excitation (unit cell type A). For experimental results, $\ddot{x}_{\text{out}} = \ddot{x}_3^{\text{ex}}$, $\ddot{x}_{\text{in}} = \ddot{x}_5^{\text{ex}}$. For numerical results, $\ddot{x}_{\text{out}} = \ddot{y}_3^{\text{num}}$, $\ddot{x}_{\text{in}} = \ddot{x}_g$.

VI. CONCLUSIONS

The current study investigates the dynamic behavior and vibration-mitigation properties of a metamaterial, designed to exploit geometric nonlinearities. This is studied via both an analytical and a numerical approach, resulting in an agreement between the two methods. The dispersion relation reveals the amplitude-dependent band gaps that can be tuned acting on a few design parameters. The dynamic response of the nonlinear metamaterial is further validated on the basis of experimental testing. For this purpose, a one-dimensional lattice is assembled and studied under one-dimensional dynamic loading. Experimental results reveal the vibration-mitigation capabilities of the system both in terms of investigating the band-gap dependence on amplitude, as well as the vibration attenuation effect on a primary system. Promising observations are made on the potential of the nonlinear designs in mitigating the effect of dynamic loading to this protected structure. Finally, in order to evaluate the conformity of the modeling assumptions and the physical observations, numerical simulations of the time history, and frequency response corresponding to the physical configuration are performed.

The vibration-mitigation capabilities of the investigated nonlinear metamaterial configuration reveal promising results. The negative stiffness properties allow the band-gap opening to shift into very low frequencies without adding substantial mass as it is done for linear design. The presence of nonlinearity is responsible for the translation of the attenuation zone in the frequency domain, while it additionally affects the width of the band gap. This appears significantly widened for high oscillation amplitudes. Throughout the evolution of a dynamic loading event, the configuration experiences numerous alterations in the oscillation amplitude, which has the effect of constantly updating the band-gap range, essentially influencing additional frequencies.

While this is an initial investigation, validated by a scaled proof-of-concept system, the feasibility of the design and further practical limitations should be further investigated prior to proceeding to a realistic full-scale application. The practical implementation aspects of the proposed design for seismic protection of structures are currently under investigation. The objective is to introduce the nonlinear metamaterial setup in the lateral support of a system, mitigating vibrations within the attenuation zone. The triangular arch can be composed by a set of spring or truss and viscous damper elements. For structural applications, the 2L dimension of the arch is expected to amount to roughly 1 m, where a placement of three cells in the vertical direction covers a 3-m typical floor height. The anticipated displacement level of the excitation should determine dimension H , which for seismic events can be estimated to 0.1 m. To simplify assembly, we consider the stiff support of each cell to be comprised of reinforced concrete, allowing on-site fabrication. Preliminary analyses

demonstrate the efficacy of a three-cell configuration, with the aforementioned properties, in limiting the response to a structure, in the presence of soil-structure interaction and are planned to be thoroughly explored and included in a future feasibility study. A critical aspect that needs to be resolved for real applications is the design of the joints, which must provide rotational freedom to the spring elements, while being able to withstand large loads without failing.

ACKNOWLEDGMENTS

This project has received funding from the European Union's Horizon 2020 research and innovation programme under the Marie Skłodowska-Curie Grant Agreement No. 813424-INSPIRE. A.C. is supported by the H2020 FETOpen project BOHEME under Grant Agreement No. 863179 and by the SNSF Ambizione Fellowship PZ00P2-174009.

APPENDIX: NUMERICAL ALGORITHM FOR THE CALCULATION OF THE NONLINEAR EQUILIBRIUM PATH INCORPORATING SUPPORT ELASTICITY

Equation (A1) describe the process of calculating the values of $\delta_{j,i}$, $r_{j,i}$, $P_{j,i} = F_{nl}^{j,i}$ for the j th unit cell at step i considering the elasticity of the supporting members in the form of their stiffness k_f . Provided that the displacement step $d\delta_{j,i}$ is sufficiently small, and that the system initiates from an equilibrium position, the nonlinear equilibrium path can be calculated.

$$\begin{aligned}
 &\delta_{j,0} = 0, r_{j,0} = 0, P_{j,0} = 0, \\
 &L_{j,0} = L = L_o, H_{j,0} = H = H_o, \\
 &\quad \downarrow \\
 &\delta_{j,1} = \delta_{j,0} + d\delta_{j,1} \rightarrow \varphi_{j,1} = \arctan\left(\frac{H_o - \delta_{j,1}}{L_o + r_{j,0}}\right), \\
 &P_{j,1} = P(L_{j,0}, H_{j,0}, \delta_{j,1} - (H_o - H_{j,0}), k_f) = 2N_{j,1}^y, \\
 &\quad N_{j,1}^z = N_{j,1}^y / \tan \varphi_{j,1}, \\
 &\quad r_{j,1} = N_{j,1}^z / k_f, \\
 &\quad L_{j,1} = L_o + r_{j,1}, \\
 &H_{j,1} = \sqrt{H_o^2 + L_o^2 - L_{j,1}^2}, \\
 &\quad \downarrow \\
 &\dots \\
 &\quad \downarrow
 \end{aligned} \tag{A1}$$

$$\begin{aligned}
 \delta_{j,i} &= \delta_{j,i-1} + d\delta_{j,i} \rightarrow \varphi_{j,i} = \arctan\left(\frac{H_o - \delta_{j,i}}{L_o + r_{j,i-1}}\right), \\
 P_{j,i} &= P(L_{j,i-1}, H_{j,i-1}, \delta_{j,i} - (H_o - H_{j,i-1}), k_f) = 2N_{j,i}^y, \\
 N_{j,i}^z &= N_{j,i}^y / \tan \varphi_{j,i}, \\
 r_{j,i} &= N_{j,i}^z / k_f, \\
 L_{j,i} &= L_o + r_{j,i}, \\
 H_{j,i} &= \sqrt{H_o^2 + L_o^2 - L_{j,i}^2},
 \end{aligned}$$

where $P_{j,i}$ is calculated from Eq. (1).

-
- [1] A. K. Chopra, *Dynamics of Structures: Theory and Applications to Earthquake Engineering*, 4th Ed. (Pearson, Harlow, England, 2014).
 - [2] S. L. Kramer, *Geotechnical Earthquake Engineering* (Prentice Hall, Upper Saddle River, New Jersey, USA, 1996).
 - [3] V. A. Matsagar and R. S. Jangid, Base isolation for seismic retrofitting of structures, *Pract. Period. Struct. Des. Constr.* **13**, 175 (2008).
 - [4] M. S. Miah, E. N. Chatzi, V. K. Dertimanis, and F. Weber, Real-time experimental validation of a novel semi-active control scheme for vibration mitigation, *Struct. Control Heal. Monit.* **24**, e1878 (2017).
 - [5] F. Fraternali, N. Singh, A. Amendola, G. Benzoni, and G. W. Milton, A biomimetic sliding-stretching approach to seismic isolation, *Nonlinear Dyn.* **106**, 3147 (2021).
 - [6] A. Y. Tuan and G. Q. Shang, Vibration control in a 101-storey building using a tuned mass damper, *J. Appl. Sci. Eng.* **17**, 141 (2014).
 - [7] Z. Zhou, X. Wei, Z. Lu, and B. Jeremic, Influence of soil-structure interaction on performance of a super tall building using a new eddy-current tuned mass damper, *Struct. Des. Tall Spec. Build.* **27**, e1501 (2018).
 - [8] P. Banerji, M. Murudi, A. H. Shah, and N. Popplewell, Tuned liquid dampers for controlling earthquake response of structures, *Earthq. Eng. Struct. Dyn.* **29**, 587 (2000).
 - [9] R. O. Ruiz, D. Lopez-Garcia, and A. A. Taflanidis, Modeling and experimental validation of a new type of tuned liquid damper, *Acta Mech.* **227**, 3275 (2016).
 - [10] S. Suresh, S. Narasimhan, S. Nagarajaiah, and N. Sundararajan, Fault-tolerant adaptive control of nonlinear base-isolated buildings using EMRAN, *Eng. Struct.* **32**, 2477 (2010).
 - [11] R. V. Craster and S. Guenneau, eds., *Acoustic Metamaterials* (Springer, Dordrecht, 2013).
 - [12] F. Bilotti and L. Sevgi, Metamaterials: Definitions, properties, applications, and FDTD-based modeling and simulation (invited paper), *Int. J. RF Microw. Comput. Eng.* **22**, 422 (2012).
 - [13] V. Fedotov, in *Springer Handbooks* (Springer, Cham, 2017).
 - [14] L. Liu and M. I. Hussein, Wave motion in periodic flexural beams and characterization of the transition between

- Bragg scattering and local resonance, *J. Appl. Mech. Trans. ASME* **79**, 011003 (2012).
- [15] M. H. Lu, L. Feng, and Y. F. Chen, Phononic crystals and acoustic metamaterials, *Mater. Today* **12**, 34 (2009).
- [16] R. Martínez-Sala, J. Sancho, J. V. Sánchez, V. Gómez, J. Llinares, and F. Meseguer, Sound attenuation by sculpture, *Nature* **378**, 241 (1995).
- [17] A. Palermo, S. Krödel, K. H. Matlack, R. Zaccherini, V. K. Dertimanis, E. N. Chatzi, A. Marzani, and C. Daraio, Hybridization of Guided Surface Acoustic Modes in Unconsolidated Granular Media by a Resonant Metasurface, *Phys. Rev. Appl.* **9**, 054026 (2018).
- [18] L. Wu, Y. Wang, K. Chuang, F. Wu, Q. Wang, W. Lin, and H. Jiang, A brief review of dynamic mechanical metamaterials for mechanical energy manipulation, *Mater. Today* **44**, 168 (2021).
- [19] V. K. Dertimanis, I. A. Antoniadis, and E. N. Chatzi, Feasibility analysis on the attenuation of strong ground motions using finite periodic lattices of mass-in-mass barriers, *J. Eng. Mech.* **142**, 04016060 (2016).
- [20] P. R. Wagner, V. K. Dertimanis, I. A. Antoniadis, and E. N. Chatzi, On the feasibility of structural metamaterials for seismic-induced vibration mitigation, *Int. J. Earthq. Impact Eng.* **1**, 20 (2016).
- [21] A. Colombi, R. Zaccherini, G. Aguzzi, A. Palermo, and E. Chatzi, Mitigation of seismic waves: Metabarriers and metafoundations bench tested, *J. Sound Vib.* **485**, 115537 (2020).
- [22] A. Franchini, O. S. Bursi, F. Basone, and F. Sun, Finite locally resonant metafoundations for the protection of slender storage tanks against vertical ground accelerations, *Smart Mater. Struct.* **29**, 055017 (2020).
- [23] R. Zaccherini, A. Palermo, S. Krödel, V. K. Dertimanis, A. Marzani, C. Daraio, and E. N. Chatzi, in *Proc. ISMA 2018—Int. Conf. Noise Vib. Eng. USD 2018—Int. Conf. Uncertain. Struct. Dyn.* (KU Leuven - Departement Werktuigkunde, Leuven, 2018), p. 3047.
- [24] R. Zaccherini, A. Palermo, A. Marzani, A. Colombi, V. Dertimanis, and E. Chatzi, Mitigation of Rayleigh-like waves in granular media via multi-layer resonant metabarriers, *Appl. Phys. Lett.* **117**, 254103 (2020).
- [25] A. Palermo, S. Krödel, A. Marzani, and C. Daraio, Engineered metabarrier as shield from seismic surface waves, *Sci. Rep.* **6**, 39356 (2016).
- [26] M. Miniaci, A. Krushynska, F. Bosia, and N. M. Pugno, Large scale mechanical metamaterials as seismic shields, *New J. Phys.* **18**, 083041 (2016).
- [27] M. Wenzel, F. Basone, and O. S. Bursi, Design of a metamaterial-based foundation for fuel storage tanks and experimental evaluation of its effect on a connected pipeline system, *J. Press. Vessel Technol.* **142**, 021903 (2020).
- [28] M. Wenzel, O. S. Bursi, and I. Antoniadis, Optimal finite locally resonant metafoundations enhanced with nonlinear negative stiffness elements for seismic protection of large storage tanks, *J. Sound Vib.* **483**, 115488 (2020).
- [29] M. H. Bae and J. H. Oh, Amplitude-induced bandgap: New type of bandgap for nonlinear elastic metamaterials, *J. Mech. Phys. Solids* **139**, 103930 (2020).
- [30] C. Daraio, V. F. Nesterenko, E. B. Herbold, and S. Jin, Tunability of solitary wave properties in one-dimensional strongly nonlinear phononic crystals, *Phys. Rev. E* **73**, 026610 (2006).
- [31] X. Fang, J. Wen, B. Bonello, J. Yin, and D. Yu, Ultra-low and ultra-broad-band nonlinear acoustic metamaterials, *Nat. Commun.* **8**, 1 (2017).
- [32] R. Zivieri, F. Garesci, B. Azzerboni, M. Chiappini, and G. Finocchio, Nonlinear dispersion relation in anharmonic periodic mass-spring and mass-in-mass systems, *J. Sound Vib.* **462**, 114929 (2019).
- [33] A. Mojahed, J. Bunyan, S. Tawfick, and A. F. Vakakis, Tunable Acoustic Nonreciprocity in Strongly Nonlinear Waveguides with Asymmetry, *Phys. Rev. Appl.* **12**, 034033 (2019).
- [34] X. Xu, M. V. Barnhart, X. Fang, J. Wen, Y. Chen, and G. Huang, A nonlinear dissipative elastic metamaterial for broadband wave mitigation, *Int. J. Mech. Sci.* **164**, 105159 (2019).
- [35] P. Martakis, G. Aguzzi, V. K. Dertimanis, E. N. Chatzi, and A. Colombi, Nonlinear periodic foundations for seismic protection: Practical design, realistic evaluation and stability considerations, *Soil Dyn. Earthq. Eng.* **150**, 106934 (2021).
- [36] W. Jiao and S. Gonella, Intermodal and Subwavelength Energy Trapping in Nonlinear Metamaterial Waveguides, *Phys. Rev. Appl.* **10**, 024006 (2018).
- [37] K. A. I. Chondrogiannis, V. K. Dertimanis, S. F. Masri, and E. N. Chatzi, 6 in *Proc. Int. Conf. Struct. Dyn., EURO Dyn* (European Association for Structural Dynamics, Virtual, Athens, 2020), p. 4139.
- [38] A. Banerjee, E. P. Calius, and R. Das, An impact based mass-in-mass unit as a building block of wideband nonlinear resonating metamaterial, *Int. J. Nonlinear Mech.* **101**, 8 (2018).
- [39] A. Banerjee, E. P. Calius, and R. Das, Impact based wideband nonlinear resonating metamaterial chain, *Int. J. Nonlinear Mech.* **103**, 138 (2018).
- [40] M. Hwang and A. F. Arrieta, Extreme Frequency Conversion from Soliton Resonant Interactions, *Phys. Rev. Lett.* **126**, 073902 (2021).
- [41] M. A. Al-Shudeifat, Highly efficient nonlinear energy sink, *Nonlinear Dyn.* **76**, 1905 (2014).
- [42] Y. Chen, Z. Qian, K. Chen, P. Tan, and S. Tesfamariam, Seismic performance of a nonlinear energy sink with negative stiffness and sliding friction, *Struct. Control Heal. Monit.* **26**, e2437 (2019).
- [43] S. Chen, B. Wang, S. Zhu, X. Tan, J. Hu, X. Lian, L. Wang, and L. Wu, A novel composite negative stiffness structure for recoverable trapping energy, *Compos. Part A Appl. Sci. Manuf.* **129**, 105697 (2020).
- [44] L. Salari-Sharif, B. Haghighpanah, A. Guell Izard, M. Tootk-aboni, and L. Valdevit, Negative-Stiffness Inclusions as a Platform for Real-Time Tunable Phononic Metamaterials, *Phys. Rev. Appl.* **11**, 024062 (2019).
- [45] I. A. Antoniadis and A. Paradeisiotis, Acoustic metamaterials incorporating the KDamper concept for low frequency acoustic isolation, *Acta Acust. United Acust.* **104**, 636 (2018).

- [46] K. A. Kapasakalis, I. A. Antoniadis, and E. J. Sapountzakis, Performance assessment of the KDamper as a seismic absorption base, *Struct. Control Heal. Monit.* **27**, e2482 (2020).
- [47] A. Paradeisiotis, M. Kalderon, and I. Antoniadis, Advanced negative stiffness absorber for low-frequency noise insulation of panels, *AIP Adv.* **11**, 065003 (2021).
- [48] H. H. Huang, C. T. Sun, and G. L. Huang, On the negative effective mass density in acoustic metamaterials, *Int. J. Eng. Sci.* **47**, 610 (2009).
- [49] M. I. Hussein and M. J. Frazier, Metadamping: An emergent phenomenon in dissipative metamaterials, *J. Sound Vib.* **332**, 4767 (2013).
- [50] G. Arioli and F. Gazzola, Periodic motions of an infinite lattice of particles with nearest neighbor interaction, *Nonlinear Anal. Theory Methods Appl.* **26**, 1103 (1996).
- [51] P. J. Torres, Periodic motions of forced infinite lattices with nearest neighbor interaction, *Z. Angew. Math. Phys. ZAMP* **51**, 333 (2000).
- [52] C. Wang and D. Qian, Periodic motions of a class of forced infinite lattices with nearest neighbor interaction, *J. Math. Anal. Appl.* **340**, 44 (2008).
- [53] C. Kittel, *Introduction to Solid State Physics* (John Wiley & Sons, New York, 2004), 8th ed, p. 704.
- [54] M. Collet, M. Ouisse, M. Ruzzene, and M. N. Ichchou, Floquet-Bloch decomposition for the computation of dispersion of two-dimensional periodic, damped mechanical systems, *Int. J. Solids Struct.* **48**, 2837 (2011).
- [55] A. Palermo and A. Marzani, A reduced Bloch operator finite element method for fast calculation of elastic complex band structures, *Int. J. Solids Struct.* **191–192**, 601 (2020).
- [56] M. A. Campana, M. Ouisse, E. Sadoulet-Reboul, M. Ruzzene, S. Neild, and F. Scarpa, Impact of non-linear resonators in periodic structures using a perturbation approach, *Mech. Syst. Signal Process.* **135**, 106408 (2020).
- [57] G. Chakraborty and A. K. Mallik, Dynamics of a weakly non-linear periodic chain, *Int. J. Nonlinear Mech.* **36**, 375 (2001).
- [58] X. Fang, J. Wen, J. Yin, and D. Yu, Wave propagation in nonlinear metamaterial multi-atomic chains based on homotopy method, *AIP Adv.* **6**, 121706 (2016).
- [59] X. Fang, J. Wen, J. Yin, D. Yu, and Y. Xiao, Broadband and tunable one-dimensional strongly nonlinear acoustic metamaterials: theoretical study, *Phys. Rev. E* **94**, 052206 (2016).
- [60] B. S. Lazarov and J. S. Jensen, Low-frequency band gaps in chains with attached non-linear oscillators, *Int. J. Nonlinear Mech.* **42**, 1186 (2007).
- [61] M. Krack and J. Gross, *Harmonic Balance for Nonlinear Vibration Problems*, Mathematical Engineering (Springer International Publishing, Cham, 2019), p. 159.
- [62] M. I. Hussein, M. J. Leamy, and M. Ruzzene, Dynamics of phononic materials and structures: Historical origins, recent progress, and future outlook, *Appl. Mech. Rev.* **66**, 040802 (2014).
- [63] E. Pennestri, V. Rossi, P. Salvini, and P. P. Valentini, Review and comparison of dry friction force models, *Nonlinear Dyn.* **83**, 1785 (2016).
- [64] D. Alleyne and P. Cawley, A two-dimensional Fourier transform method for the measurement of propagating multimode signals, *J. Acoust. Soc. Am.* **89**, 1159 (1991).
- [65] M. Kutz, ed., *Handbook of Materials Selection* (John Wiley & Sons, Inc., New York, 2002).